Optical bistability with hybrid silicon-plasmonic disk resonators

Odysseas Tsilipakos[1,*] and Emmanouil E. Kriezis[1]

[1] *Department of Electrical and Computer Engineering, Aristotle University of Thessaloniki, Thessaloniki GR-54124, Greece*

compiled: May 31, 2014

Optical bistability with a hybrid silicon-plasmonic configuration consisting of a nonlinear traveling-wave (disk) resonator side-coupled with a bus waveguide is theoretically investigated. The nonlinear response is studied with a theoretical framework combining perturbation theory and temporal coupled-mode theory. For the CW case, a general closed-form expression is derived. The effect of the parameters entering in the expression on the bistability curve is thoroughly investigated and the physical system is accordingly designed so as to exhibit minimum power threshold for bistability and maximum extinction ratio between bistable states. Finally, the temporal dynamics are assessed. The system can toggle between bistable states in approximately 5 ps and is thus suitable for ultrafast memory/switching applications.

OCIS codes: 130.4310, 190.1450, 190.4390, 230.4320, 250.5403

1. Introduction

Guided-wave plasmonic circuits have attracted considerable attention in recent years. An abundance of passive components has been demonstrated based on diverse waveguiding configurations [1]. Gradually, interest is shifting towards dynamic/tunable components, since they are essential for assembling circuits with high levels of functionality. Several tuning mechanisms have been utilized for this purpose including thermo-optic [2], electro-optic [3], and nonlinear [4] effects. In particular, nonlinear phenomena based on the third order susceptibility, $\chi^{(3)}$, can be a favorable approach, since they feature ultrafast response times (the Kerr effect is characterized as instantaneous) and moreover allow for all-optical operation, thus eliminating the need for electrical control signals.

A straightforward approach for implementing switching elements by exploiting $\chi^{(3)}$ nonlinearity is the nonlinear directional coupler. Indeed, such components have already been demonstrated with semiconductor-loaded [5], gap [6], and hybrid [7] plasmonic waveguides. However, due to the significant propagation (resistive) losses of plasmonic waveguides leading to short interaction lengths, the input power required for switching is very high. An alternative approach is to employ a nonlinear resonator coupled to a bus waveguide. The combination of nonlinearity and optical feedback results in bistable behavior, which in turn offers a route towards implementing memory or switching elements [8]. Importantly, the intensity build-up in the resonator results in higher power densities, thus leading to reduced input power requirements for switching. However, to date relevant studies are limited to two-dimensional geometries with the metal-insulator-metal (MIM) waveguide [9–12].

In this work, we address the need for practical, three-dimensional bistable plasmonic components. More specifically, among the configurations capable of exhibiting optical bistability we examine the system consisting of a nonlinear traveling-wave (disk) resonator side-coupled to an access waveguide. The manifestation of nonlinear effects in general, and bistability in particular, requires strong mode confinement and low losses. We therefore base the design on the conductor-gap-silicon (CGS) hybrid plasmonic waveguide [13], which allows for nanoscale mode confinement and, at the same time, relatively low propagation losses. The nonlinear response of the disk-waveguide system is studied by means of a theoretical model combining perturbation theory and temporal coupled-mode theory (CMT), fed with rigorous, full-wave simulations of the linear system conducted with the three-dimensional vectorial finite element method (3D-VFEM). Based on the simulation results, we identify the geometrical parameters leading to optimum performance in terms of input power threshold and extinction ratio (ER) between bistable states. We show that the resonator approach leads to reduced input power requirements compared to a nonlinear directional coupler implementation. The response time is limited by the photon lifetime in the cavity, which, however, is in the order of a few ps, thus allowing for extremely high operating speeds.

The paper is organized as follows: The material and geometrical parameters of the system under study are presented in Section 2. In Section 3 the theoretical framework is introduced and a general *closed-form* expression describing the CW nonlinear response is de-

* Corresponding author: otsilipa@auth.gr

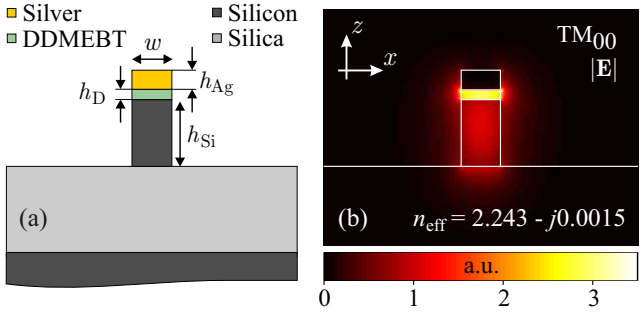

Fig. 1. (a) Cross-section of nonlinear CGS waveguide. The gap between silver and silicon layers is occupied by the nonlinear polymer DDMEBT. The heights of the three layers comprising the guiding ridge (silver, DDMEBT, Si) are $h_{\mathrm{Ag}} = 100$ nm, $h_{\mathrm{D}} = 50$ nm, and $h_{\mathrm{Si}} = 340$ nm, respectively. The waveguide width w is 200 nm. (b) Distribution of electric field norm for the fundamental mode (TM_{00}) at 1.55 μm.

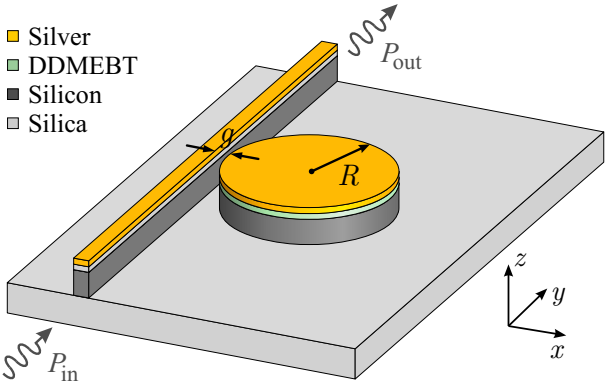

Fig. 2. NLCGS-based disk resonator coupled to a CGS bus waveguide through coupling gap g.

rived, valid for finite intrinsic quality factors and arbitrary coupling conditions. The effect of the parameters entering in the theoretical model, namely, the detuning $\bar{\delta}$ and quality factor ratio r_Q, on the bistability curve are investigated in Section 4. Based on the findings of this Section, we design the physical system in Section 5 and assess its performance in terms of required input power, extinction ratio between bistable states, and response time. Finally, a discussion on future directions is provided in the concluding Section 6.

2. Nonlinear disk structure

The system considered is based on the nonlinear conductor-gap-silicon (NLCGS) waveguide introduced in [14]. The waveguide cross-section is depicted in Fig. 1(a). It is similar to a standard CGS waveguide [13], with the exception that a nonlinear polymer is occupying the low-index "gap" between high-index semiconductor and metal regions, instead of silica. More specifically, the polymer of choice is DDMEBT [15], which apart from being highly nonlinear ($n_2 = 1.7 \times 10^{-17}$ m^2/W) has moreover proven compatible with nanophotonic integration [16]. The metal is silver, since it features lower resistive losses compared to gold, which is of paramount importance in nonlinear applications. The linear refractive indices for the considered materials at the telecom wavelength of 1.55 μm are $n_{\mathrm{SiO_2}} = 1.45$, $n_{\mathrm{Si}} = 3.48$, $n_{\mathrm{DDMEBT}} = 1.8$, and $n_{\mathrm{Ag}} = 0.145 - j11.4$ [17].

Regarding geometrical parameters, the dimensions of the silicon core are $w \times h_{\mathrm{Si}} = 200$ nm$\times$340 nm, typical for CGS waveguides [13]. Importantly, the 340-nm height is customary for silicon photonic waveguides operating on the TM mode, thus facilitating the interfacing of the CGS waveguide with standard silicon photonic circuitry. The polymer layer is 50-nm high, a favorable compromise between mode confinement and propagation loss, while for the silver layer $h_{\mathrm{Ag}} = 100$ nm.

The fundamental TM mode supported by the NLCGS waveguide is depicted in Fig. 1(b). More specifically, we plot the electric field norm ($|\mathbf{E}|$), as obtained with a FEM eigenmode solver. Notice that the electric field is approximately three times stronger in the nonlinear material compared to the silicon core. In fact, the mode is almost entirely located inside the nanosized polymer layer. The effective mode area, calculated through $A_{\mathrm{eff}} \triangleq (\iint |\mathbf{E}|^2 \,\mathrm{d}x\mathrm{d}y)^2 / \iint |\mathbf{E}|^4 \,\mathrm{d}x\mathrm{d}y$, is only 0.052 μm^2. Except from enhancing the power density, strong confinement allows for implementing compact resonators with negligible radiation loss, meaning that the NLCGS waveguide is particularly well suited to our application. The effective index at 1.55 μm is $n_{\mathrm{eff}} = 2.243 - j0.0015$, with the imaginary part corresponding to a propagation length (the e-folding distance of the optical intensity) of $L_{\mathrm{prop}} = 80$ μm. On the whole, the considered waveguide can provide subwavelength confinement while maintaining propagation loss at a relatively low level.

Given the excellent overlap of the supported mode with the nonlinear material [Fig. 1(b)] and the high nonlinear index of DDMEBT, the waveguide is anticipated quite nonlinear. Indeed, by employing the definition in [18] the nonlinear coefficient γ_{wg} is found equal to 1535 W^{-1}m^{-1}. Note that although silicon possesses a relatively high nonlinearity as well ($n_2^{\mathrm{Si}} = 2.5 \times 10^{-18}$ m^2/W), waveguide nonlinearity stems solely from the polymer. Despite this high γ_{wg} value, switching operation with a directional coupler approach would require high input powers in the order of 44 W, estimated through $P_{\mathrm{sw}} = \pi\sqrt{3}/(\gamma_{\mathrm{wg}} L_{\mathrm{prop}})$ [7]. As mentioned in Section 1, this is due to the significant resistive losses ($L_{\mathrm{prop}} = 80$ μm) resulting in extremely short lengths for nonlinear interaction.

It is thus expedient to investigate whether an approach based on a resonant configuration exhibiting optical bistability can lower the input power required for switching. Something like this is actually anticipated due to the intensity build-up in the resonator. The structure examined is depicted in Fig. 2. More specifically, we form a disk resonator based on the NLCGS waveg-

uide structure and side-couple it with a standard CGS waveguide ($w = 200$ nm). We opt for a disk instead of a microring resonator since it features higher quality factors, especially in small-radius cases where radiation losses are the dominant loss mechanism (as compared to resistive ones) [19, 20]. As will become evident in Section 3, we are seeking resonant modes with small effective volumes, meaning that we are interested in exactly this small-radius regime. In addition, the input power threshold for bistability scales with $1/Q^2$ meaning that disk superiority concerning quality factors becomes very relevant. We note that a donut resonator can be also employed with the purpose of suppressing unwanted higher-radial-order or "photonic" modes of the disk [20], in the event of such resonances cluttering the optical response.

3. Theoretical framework

The nonlinear response of the disk-waveguide system is studied with a theoretical framework combining perturbation theory and temporal coupled-mode theory [21]. This approach is much simpler compared to rigorously simulating the three-dimensional nonlinear system and still produces very accurate results, as has been demonstrated with photonic crystal cavities [21–24]. Rigorous full-wave simulations of the 3D system still need to be performed in order to feed the theoretical model, albeit they concern the linear system. In this work, these simulations are conducted with the 3D-VFEM [25].

Although the framework is generally well known, especially in the case of standing-wave resonators, in this Section we briefly outline the formulation for the purpose of deriving a general *closed-form* expression, valid for finite intrinsic quality factors and arbitrary coupling conditions, describing the CW nonlinear response. In the process, we take care in highlighting the points requiring attention. First, by applying perturbation theory, namely, approximating the perturbed fields with the unperturbed ones, the resonant frequency shift $\Delta\omega$ of a cavity perturbed by nonlinear self-action can be cast in the following form [21]

$$\frac{\Delta\omega}{\omega_0} = -c_0 \left(\frac{\omega_0}{c_0}\right)^3 \kappa\, n_2^{\max}\, W, \tag{1}$$

where $W = (\varepsilon_0/2)\iiint_V n^2(\mathbf{r})\mathbf{E}_0 \cdot \mathbf{E}_0^*\,\mathrm{d}V$ with $\mathbf{E}_0$ denoting the unperturbed electric field in the structure (the coordinate dependence is suppressed). Since on resonance the electric and magnetic field energies are equal, W amounts to the total energy stored in the resonator ($W_e + W_m = 2W_e = W$), meaning that the nonlinear resonant frequency shift is proportional to the stored energy. κ is the nonlinear feedback parameter defined through

$$\kappa \triangleq \left(\frac{c_0}{\omega_0}\right)^3 \times \frac{\iiint_V \frac{1}{3} n_2(\mathbf{r}) n^2(\mathbf{r}) \left[(\mathbf{E}_0 \cdot \mathbf{E}_0)(\mathbf{E}_0^* \cdot \mathbf{E}_0^*) + 2|\mathbf{E}_0|^4\right] \mathrm{d}V}{\left[\iiint_V n^2(\mathbf{r})\mathbf{E}_0 \cdot \mathbf{E}_0^*\,\mathrm{d}V\right]^2 n_2^{\max}}, \tag{2}$$

with $n_2^{\max}$ being the maximum value of $n_2(\mathbf{r})$ anywhere in the structure. It is a dimensionless parameter measuring the degree of overlap between the supported mode and the nonlinear material. In addition, κ is inversely proportional to the effective modal volume (V_{eff}), which can be verified by comparing Eq. (2) with the following definition [26]

$$V_{\text{eff}} \triangleq \frac{\left(\iiint_V \varepsilon(\mathbf{r})\,|\mathbf{E}(\mathbf{r})|^2\ \mathrm{d}V\right)^2}{\iiint_V \varepsilon(\mathbf{r})^2\,|\mathbf{E}(\mathbf{r})|^4\ \mathrm{d}V}. \tag{3}$$

The analogy becomes obvious if we assume a scalar field in which case the bracketed quantity in the nominator of Eq. (2) becomes $3|E_0|^4$. Finally, in Eq. (1) ω_0 is the unperturbed resonant frequency and c_0 the speed of light in vacuum. The minus sign indicates that the frequency shift due to nonlinear self-action is towards lower frequencies (redshift) in the customary case of self-focusing ($n_2 > 0$) materials.

Now, according to temporal coupled-mode theory [27–29] a system consisting of a traveling-wave resonator side-coupled to a bus waveguide is described by

$$\frac{\mathrm{d}a}{\mathrm{d}t} = j(\omega_0 + \Delta\omega)a - \frac{1}{\tau_i}a - \frac{1}{\tau_e}a + j\sqrt{\frac{2}{\tau_e}}s_i, \tag{4}$$

where τ_i, τ_e denote photon lifetimes corresponding to intrinsic and coupling (external) losses, respectively. They are associated with the respective quality factors through $Q = \omega_0\tau/2$. Note that the resonant frequency ω_0 is perturbed by the nonlinear frequency shift $\Delta\omega$. s_i denotes the incident wave amplitude and is related to the transmitted (past the resonator) wave amplitude s_t through

$$s_t = s_i + j\sqrt{\frac{2}{\tau_e}}a. \tag{5}$$

Amplitudes $s_{i,t}$ are normalized so that $|s_{i,t}|^2$ express guided power. In the same way, the cavity amplitude a is normalized so that $|a|^2$ is the energy stored in the resonator ($|a|^2 \equiv W$).

Assuming a harmonic time dependence ($\exp\{j\omega t\}$) the steady-state response (transmission) is given by

$$t = \frac{s_t}{s_i} = \frac{j(\omega - \omega_0 - \Delta\omega) + \left(\frac{1}{\tau_i} - \frac{1}{\tau_e}\right)}{j(\omega - \omega_0 - \Delta\omega) + \left(\frac{1}{\tau_i} + \frac{1}{\tau_e}\right)}. \tag{6}$$

By multiplying both nominator and denominator of Eq. (6) with τ_i we can cast the power transmission in the following form

$$T = |t|^2 = \frac{P_{\rm out}}{P_{\rm in}} = \frac{(1-r_Q)^2 + (\bar{\delta} - \tau_i \Delta\omega)^2}{(1+r_Q)^2 + (\bar{\delta} - \tau_i \Delta\omega)^2}, \quad (7)$$

where $\bar{\delta} = \tau_i(\omega - \omega_0)$ is the normalized detuning and $r_Q = \tau_i/\tau_e = Q_i/Q_e$ the ratio between internal and external quality factors.

Equation (7) associates the input and output powers. However, it cannot be used to obtain the hysterisis loop, since the nonlinear frequency shift $\Delta\omega$ depends on the stored energy W. To this end, we must express W as a function of $P_{\rm in}$ and/or $P_{\rm out}$. More specifically, by making use of the standard definition for the quality factor as energy stored over dissipated energy per optical cycle we can associate the internal resonator losses (radiation and resistive) with the intrinsic quality factor through $Q_i = \omega_0 W/P_{\rm int.loss}$. In the absence of reflection in the bus waveguide, i.e., assuming that a single unidirectional mode is circulating in the traveling-wave resonator, the dissipated power in the resonator is given by $P_{\rm int.loss} = P_{\rm in} - P_{\rm out}$. We can thus arrive at

$$W = Q_i \frac{P_{\rm in} - P_{\rm out}}{\omega_0}. \quad (8)$$

Making use of Eqs. (1) and (8) the term $\tau_i \Delta\omega$ appearing in Eq. (7) becomes

$$\tau_i \Delta\omega = -\frac{P_{\rm in} - P_{\rm out}}{P_0}, \quad (9)$$

where

$$P_0 = \frac{1}{2\left(\frac{\omega_0}{c_0}\right)^2 \kappa\, Q_i^2\, n_2^{\max}} \quad (10)$$

is the characteristic power of the system. P_0 is associated with the threshold for the manifestation of optical bistability. Obviously, efficient operation would require minimizing P_0 or, equivalently, maximizing the product $\kappa\, Q_i^2$.

Making use of Eq. (9) and introducing the normalized powers $p_{\rm in} = P_{\rm in}/P_0$ and $p_{\rm out} = P_{\rm out}/P_0$, Eq. (7) finally becomes

$$\frac{p_{\rm out}}{p_{\rm in}} = \frac{(1-r_Q)^2 + (\bar{\delta} + p_{\rm in} - p_{\rm out})^2}{(1+r_Q)^2 + (\bar{\delta} + p_{\rm in} - p_{\rm out})^2}. \quad (11)$$

Equation (11) is a simple closed-form relation which describes the optical response of a system consisting of a nonlinear traveling-wave resonator side-coupled to an access waveguide and allows for readily constructing the hysterisis loop (it can be even solved analytically as a third order polynomial). It is directly analogous to the closed-form equations derived for direct- [22] and side-coupled [23] standing-wave resonators, with the exception of being moreover generalized to handle finite Q_i values through the introduction of r_Q.

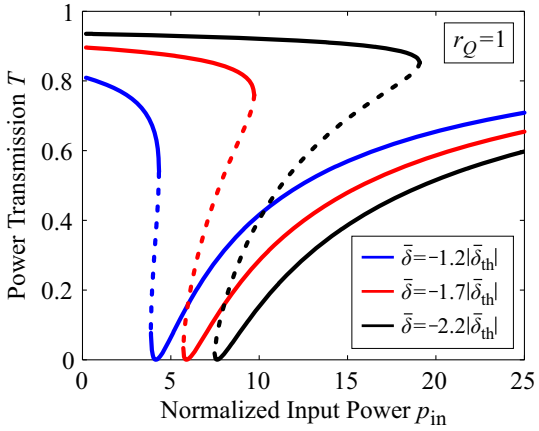

Fig. 3. Effect of normalized detuning $\bar{\delta}$ on the optical response. Power transmission is plotted as a function of $p_{\rm in}$ for $\bar{\delta} = \{-1.2|\bar{\delta}_{\rm th}|, -1.7|\bar{\delta}_{\rm th}|, -2.2|\bar{\delta}_{\rm th}|\}$ while the quality factor ratio is fixed at $r_Q = 1$ (critical coupling). As $|\bar{\delta}|$ increases bistability manifests for higher input powers.

Optical bistability manifests when Eq. (11) admits three distinct real solutions. This can happen for appropriate input power levels as long as the normalized detuning is negative and exceeds a specific threshold value: $\bar{\delta}_{\rm th} = -(1+r_Q)\sqrt{3}$. Note that the detuning threshold depends on r_Q. In the special case of critical coupling ($Q_i = Q_e \Rightarrow r_Q = 1$), which is of particular importance as will become evident in Section 4, the detuning threshold equals $2\sqrt{3}$. Obviously, $|\bar{\delta}_{\rm th}| > 2\sqrt{3}$ in the over-coupling regime ($Q_i > Q_e \Rightarrow r_Q > 1$), whereas $|\bar{\delta}_{\rm th}| < 2\sqrt{3}$ in the under-coupling regime ($Q_i < Q_e \Rightarrow r_Q < 1$).

4. Effect of model parameters on bistability curve

Let us now investigate the effect of parameters $\bar{\delta}$ and r_Q appearing in Eq. (11) on the optical response. This way we can identify the values leading to optimum performance. Obviously, we are interested in low input power thresholds for observing bistability and high extinction ratios between bistable states.

First, we examine the effect of the normalized detuning $\bar{\delta}$. For this purpose, we assume critical coupling conditions ($r_Q = 1$) and appoint different values to $\bar{\delta}$: $-1.2|\bar{\delta}_{\rm th}|$, $-1.7|\bar{\delta}_{\rm th}|$, and $-2.2|\bar{\delta}_{\rm th}|$. The results are depicted in Fig. 3, where the power transmission ($T = p_{\rm out}/p_{\rm in}$) is plotted as a function of normalized input power. Clearly, as $|\bar{\delta}|$ increases the input power threshold for bistable operation increases as well. More specifically, for $\bar{\delta} = -1.2|\bar{\delta}_{\rm th}|$ the hysterisis loop makes its appearance for an input power level of $4P_0$, whereas if $\bar{\delta} = -2.2|\bar{\delta}_{\rm th}|$ this threshold is almost doubled. Obviously, this means that detuning values close to the respective threshold are essential for efficient operation. As secondary observations, notice that higher $|\bar{\delta}|$ values increase the span of the bistable region. This means that operating the system in the bistable regime is easier; however, large deviations of the input power are required

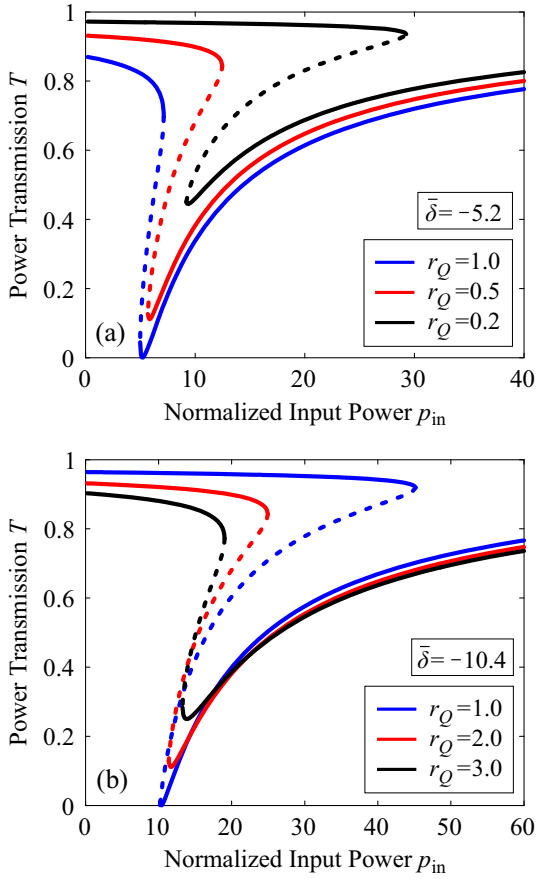

Fig. 4. Effect of quality factor ratio r_Q on the optical response. (a) $r_Q \leq 1$ regime with $\bar{\delta} = -5.2$. (b) $r_Q \geq 1$ regime with $\bar{\delta} = -10.4$. Deviating from critical coupling results in the elevation of the hysterisis loop from the zero-transmission level, leading to poor extinction ratio between bistable states.

for changing between bistable states. In addition, higher $|\bar{\delta}|$ values are associated with higher maximum transmission levels, i.e., lower insertion losses (IL $= 10 \log T_{\max}$). Finally, we stress that although Fig. 3 examines the $r_Q = 1$ case, the same trends hold for any r_Q value.

Next, we investigate the effect of r_Q on the optical response by fixing $\bar{\delta}$ at a constant value. More specifically, in Fig. 4(a) we examine the $r_Q \leq 1$ regime ($r_Q = \{1, 0.5, 0.2\}$) by setting $\bar{\delta} = -5.2$, a value corresponding to $-1.5|\bar{\delta}_{\text{th}}|$ for $r_Q = 1$: the highest value of r_Q considered. This is exercised in order to ensure that the detuning exceeds the respective threshold for all cases considered; otherwise, bistability would not manifest. We observe that a decrease in r_Q while $r_Q < 1$ results in an increase of the input power threshold for bistability. The most pronounced drawback, however, is the increase in the level of minimum transmission, translating into poor extinction ratio between bistable states. The level of maximum transmission increases as well, but on the whole their ratio decreases. It is worth noting that the minimum transmission level depends solely on the r_Q value and is not affected by the specific detuning considered; this does not hold for the maximum transmission level. Finally, one can observe that as r_Q decreases the span of the bistable region increases.

In the same way, Fig. 4(b) examines the $r_Q \geq 1$ regime ($r_Q = \{1, 2, 3\}$). The normalized detuning is set to -10.4, a value corresponding to $-1.5|\bar{\delta}_{\text{th}}|$ for $r_Q = 3$: the highest value of r_Q considered. As in the $r_Q \leq 1$ case, deviating from the critical coupling condition results in an elevation of the hysterisis loop as well as a slight increase of the input power threshold for bistability. In contrast, other less important curve characteristics follow opposite trends, since r_Q is now increasing. More specifically, the span of the bistability region decreases, as does the maximum transmission level. In any case, deviating from $r_Q = 1$ results in hysterisis loop elevation, and thus ER degradation, for both under-coupling and over-coupling cases. Therefore, satisfying the critical coupling condition is essential for efficient operation.

5. Physical system design and performance assessment

In this section, we design the physical system by utilizing the findings of Sections 3 and 4. The two geometrical parameters that need determining are the disk radius R and coupling gap g.

Our first concern is to minimize the system characteristic power P_0. For this purpose, we treat the uncoupled disk resonator (in the linear regime) as an eigenvalue problem. Solving with the 3D-VFEM we can specify the intrinsic quality factor Q_i and nonlinear feedback parameter κ [Eq. (2)], necessary for evaluating P_0 through Eq. (10). More specifically, we conduct a parametric analysis with respect to the disk radius R in order to identify the optimum value. Increasing the disk radius obviously leads to higher intrinsic quality factors (radiation losses are reduced), but at the same time the resonant mode extends over larger volumes and thus exhibits a lower feedback parameter ($\kappa \propto 1/V_{\text{eff}}$). Therefore, we are seeking the radius value which achieves the best compromise between these two opposing trends, i.e., the highest κQ_i^2 product. The disk radius is varied in the range $0.7 - 1.5$ μm and the results are depicted in Fig. 5. The possibility of exploring submicron radii is a direct consequence of the strong confinement offered by the CGS guiding structure. Note that only markers correspond to simulation results; solid lines are plotted for guiding the eye. More specifically, each of the nine markers corresponds to a resonant mode with different azimuthal order m: from $m = 6$ for $R^{\min} = 0.71$ μm to $m = 14$ for $R^{\max} = 1.47$ μm. The radius values are carefully adjusted so that the resonant wavelength is within ± 5 nm from 1.55 μm.

Figure 5(a) depicts the nonlinear feedback parameter and effective volume as functions of R. One can readily verify that the two quantities are inversely proportional, since κ decreases with radius whereas the opposite is true for V_{eff}. For the smaller radius value considered (0.71 μm), κ attains its maximum value: 5×10^{-3}. However, this does not mean that $R^{\min} = 0.71$ μm consti-

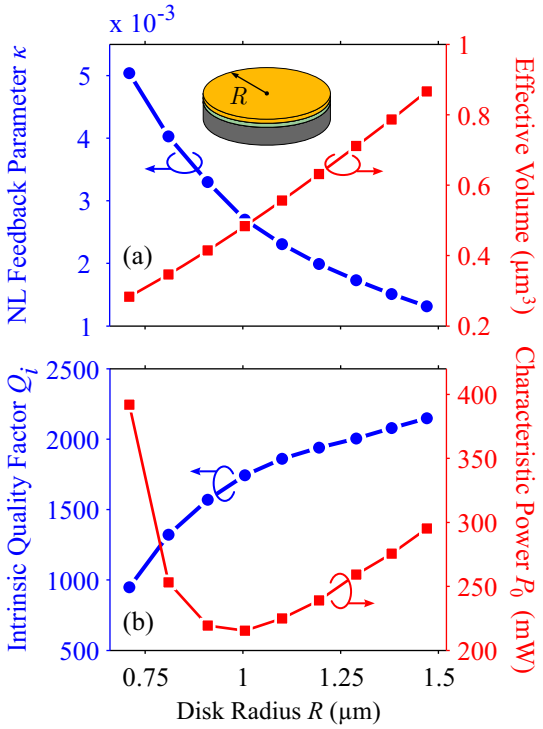

Fig. 5. Uncoupled disk resonator based on the nonlinear CGS waveguide. The system is treated as an eigenvalue problem in the linear regime with the 3D-VFEM. (a) Nonlinear feedback parameter κ and effective mode volume V_{eff} as functions of R. (b) Intrinsic quality factor Q_i and characteristic power P_0 as functions of R. The optimum radius is 1 μm corresponding to a characteristic power of 215 mW.

tutes the optimum case, since Q_i increases with radius [Fig. 5(b)] and moreover appears squared in Eq. (10). More specifically, Q_i equals 950 for $R = 0.71$ μm and peaks at 2150 for $R^{\max} = 1.47$ μm. Higher radii are not examined since Q_i is bound by resistive losses and cannot improve substantially. On the other hand, radii smaller than $R = 0.71$ μm are accompanied by significant radiation losses resulting in a steep decrease of Q_i. According to Fig. 5(b), the optimum radius is equal to approximately 1 μm and corresponds to a resonance with azimuthal order $m = 9$ and resonant wavelength 1553 nm. In this case, $\kappa = 2.7 \times 10^{-3}$, $Q_i = 1750$, and the characteristic power is at its minimum value: 215 mW. Note that if gold ($n_{\text{Au}} = 0.55 - j11.5$ [30]) was used instead of silver, the quality factor would be quite lower ($Q_i^{\text{Au}} = 500$) due to the higher level of resistive losses, resulting in a significant increase of the characteristic power: $P_0^{\text{Au}} \sim 2.5$ W. Retaining losses as low as possible is crucial for efficient operation, as with any nonlinear application. Finally, regarding the superiority of disk resonators mentioned in Section 2, we note that for the respective resonance of a NLCGS-based microring P_0 equals 370 mW.

The resonant mode featuring the minimum characteristic power ($R = 1$ μm, $m = 9$, $\lambda_{\text{res}} = 1553$ nm)

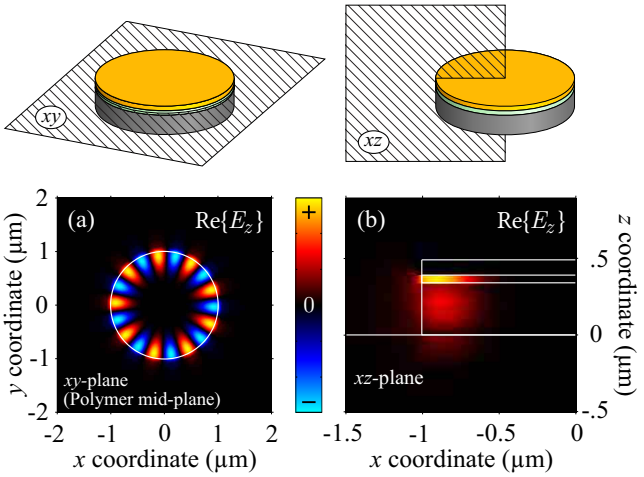

Fig. 6. Resonant mode of azimuthal order $m = 9$ for a disk resonator with $R = 1$ μm. The resonant wavelength is 1553 nm. The real part of the dominant E-field component is plotted (a) at the xy-plane halfway inside the polymer layer and (b) at the xz-plane containing the resonator axis.

is depicted in Fig. 6. More specifically, in Fig. 6(a) we plot the real part of the dominant E-field component, Re$\{E_z\}$, at the xy-plane halfway inside the polymer layer. The field is strongly confined inside the resonator, indicating that radiation losses are minimal. It is the resistive losses that are the dominant loss mechanism limiting the intrinsic quality factor to 1750. In the same way, Fig. 6(b) depicts Re$\{E_z\}$ at the xz-plane containing the resonator axis. The mode is confined inside the 50-nm polymer layer resulting in small modal volume [$V_{\text{eff}} \sim 0.48$ μm^3, Eq. (3)] and excellent overlap with the nonlinear material. Note, also, the resemblance with the fundamental mode of the waveguiding structure [Fig. 1(b)].

Having determined the optimum radius, we turn to the coupled system (Fig. 2) for the purpose of specifying the optimum coupling gap. More specifically, we are seeking the gap value that corresponds to critical coupling ($r_Q = 1$), since satisfying the critical coupling condition is critical for obtaining high ERs between bistable states as demonstrated in Section 4 (Fig. 4). As with the uncoupled case, the system is treated as an eigenvalue problem in the linear regime with the 3D-VFEM. In Fig. 7(a) we plot the loaded quality factor (Q_l) for gap values in the range $0.1 - 0.4$ μm. Clearly, Q_l increases with g, as the coupling between resonator and waveguide becomes weaker. It gradually approaches the unloaded value ($Q_i = 1750$) marked with a dashed line. By utilizing the intrinsic quality factor of the uncoupled system we can determine the external quality factor through $Q_e^{-1} = Q_l^{-1} - Q_i^{-1}$, and thus the quality factor ratio $r_Q = Q_i/Q_e$. The results are depicted for the same gap range in Fig. 7(b). Critical coupling is satisfied for a coupling gap of 225 nm. Narrower gaps lead to overcoupling ($r_Q > 1$ or $Q_i > Q_e$), whereas wider gaps to

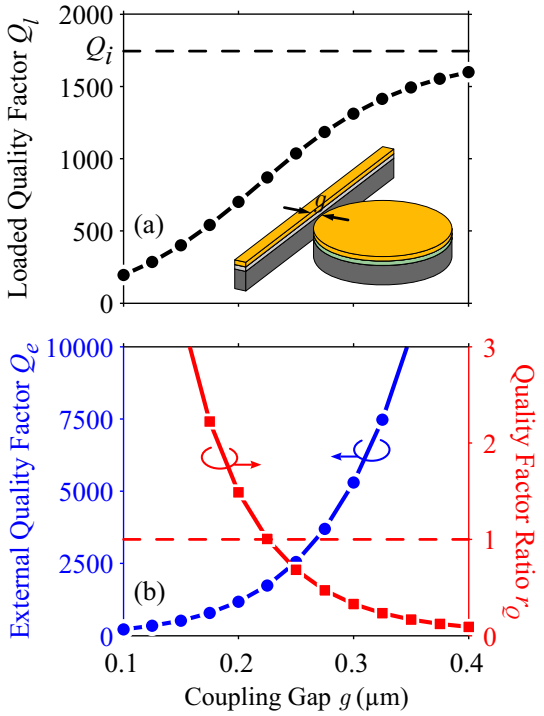

Fig. 7. NLCGS-based disk resonator coupled to CGS bus waveguide. The system is treated as an eigenvalue problem in the linear regime with the 3D-VFEM. (a) Loaded quality factor Q_l as a function of coupling gap. As the coupling gap increases, Q_l approaches the unloaded (intrinsic) value marked with a dashed line. (b) External quality factor Q_e and quality factor ratio $r_Q = Q_i/Q_e$ as functions of coupling gap. The critical couping condition is satisfied for a coupling gap of 225 nm.

under-coupling ($r_Q < 1$ or $Q_i < Q_e$).

To conclude the system design we need to specify the operating wavelength, i.e., the normalized frequency detuning $\bar{\delta}$. In Section 4 it became evident that $\bar{\delta}$ must be kept close to the respective threshold in order for the bistability loop to appear for the lowest possible input power. We therefore set $\bar{\delta} = -1.5|\bar{\delta}_{\rm th}| = -5.2$, meaning that the operating wavelength should be 2.3 nm higher than the resonant wavelength of the unperturbed resonator, i.e., equal to 1555.3 nm.

Having specified the parameters of the physical system, we can assess its performance. The bistability curve is depicted in Fig. 8. Actually, it is identical to the blue curve in Fig. 4(a), except that this time we plot the output power against $P_{\rm in}$, instead of the transmission, and de-normalize the plot axes using $P_0 = 215$ mW. Note that the hysterisis loop appears for an input power of ~ 1 W. Since the coupling gap was carefully designed so that $r_Q = 1$, there is an input power level ($P_{\rm A} = 1.12\ W$) that leads to zero output power (point A′). This means that the extinction ratio between the two bistable states A and A′ is theoretically infinite. In order to toggle between them, we can make use of the points B and C which lie beyond and below the bistability regime, re-

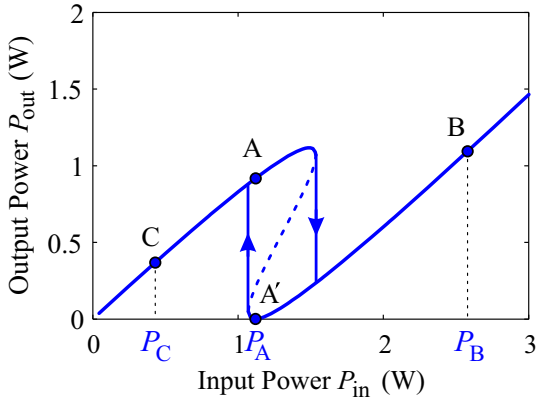

Fig. 8. Bistability curve for a 1-μm radius NLCGS disk resonator coupled to a straight CGS waveguide through a 225-nm gap. The operating wavelength is 1555.3 nm, 2.3 nm higher than the resonant wavelength of the unperturbed resonator. For $P_{\rm in} = P_{\rm A} = 1.12$ W the system exhibits bistable states A and A′ with theoretically infinite extinction ratio. Points B and C are used in Fig. 9 for toggling between them.

spectively. This is demonstrated in Fig. 9 where we investigate the dynamic response of the system by utilizing Eqs. (4) and (5). More specifically, the cavity amplitude is specified through Eq. (4), which in view of Eqs. (1), (10) can be written as

$$\frac{{\rm d}\tilde{a}}{{\rm d}t} = -j\Big(\delta + \frac{2}{\tau_i^2 P_0}|\tilde{a}|^2\Big)\tilde{a} - \frac{1}{\tau_l}\tilde{a} + j\sqrt{\frac{2}{\tau_e}}\tilde{s}_i. \qquad (12)$$

In Eq. (12) $\tilde{a}, \tilde{s}_i$ denote envelope functions and $\delta = \omega - \omega_0$. Having calculated the cavity amplitude, Eq. (5) is then used to obtain the output power. Returning to Fig. 9 the input power is initially set to $P_{\rm A} = 1.12$ W with the system resting at the high-output state (A). Note that the insertion losses in state A are quite low (~ 1 dB). This can be verified by observing the blue curve in Fig. 4(a) as well. Consequently, second-order super-Gaussian pulses with a FWHM of 2.25 ps toggle the system between bistable states. More specifically, the first pulse toggles the system to the low-output state (A′) by following the route ABA′ on the bistability curve (Fig. 8). The second pulse (actually a dip in input power) toggles the system back to the high-output state through the A′CA route. Importantly, in both cases the system settles at the new state in less than 5 ps, corresponding to approximately $3\tau_l$. (Given the loaded quality factor in the critically coupled system, $Q_l = Q_i/2 = 875$, τ_l is approximately 1.5 ps.) This means that changing the state can be performed with extremely high rates in the order of 100 GHz, rendering the proposed system suitable for ultrafast memory and/or switching applications.

6. Conclusion

To summarize, we have proposed a practical, three-dimensional hybrid silicon-plasmonic configuration capable of exhibiting optical bistability. The structure is

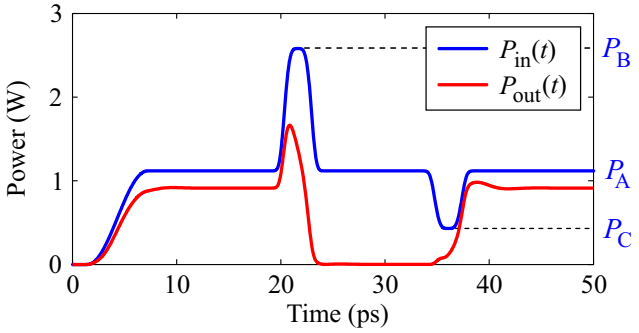

Fig. 9. Temporal response of the optimum nonlinear disk resonator system ($R = 1$ μm, $g = 225$ nm, $\lambda = 1555.3$ nm). The input power is initially set to P_A with the system resting at the high-output state (A). The first pulse toggles the system to the low-output state following the route ABA′ on the bistability curve. The second pulse toggles the system back to the high-output state through the A′CA route. In both cases, the system settles at the new state in less than 5 ps, corresponding to approximately $3\tau_l$. Points A, B, A′, and C are clearly marked in Fig. 8.

based on a side-coupled nonlinear disk resonator, it is very compact due to the strong confinement of the CGS guiding structure (footprint of approx. 4 μm^2), and can be designed to feature theoretically infinite extinction ratio between bistable states. In addition, it can be readily interfaced with standard silicon-photonic waveguides. The threshold for bistability, and thus memory/switching operation, is approximately 1 W. This constitutes a significant improvement compared to directional coupler approaches [5–7]; however, the input power is still high for telecom applications. In addition, for the said power level the electric field inside inside the nonlinear material is in the order of 100 V/μm, a rather high value approaching the breakdown voltage of typical polymer materials.

It is thus expedient to examine strategies towards lowering the bistability threshold. These include the utilization of two resonators in a cascaded configuration. In the context of photonic crystals, this has led to a three-orders-of-magnitude decrease in the required power [24]. Furthermore, one can explore other kinds of resonators, e.g., standing-wave resonators employing Bragg reflectors or photonic crystal structures for enhancing the boundary reflectivity and, thus, the resonator quality factor. Obviously, irrespective of the structure considered the nonlinear response would greatly benefit from a material with an even higher nonlinear index than DDMEBT, such as single-crystal p-toluene sulfonate (PTS) which features an index of $n_2 = 2.2\times10^{-16}$ m^2/W at 1.6 μm [31], provided that it can be processed into a thin-film and is compatible with nanophotonic integration.

We also note that thermo-optical [8, 32] or carrier-induced [33] nonlinearities can also be investigated, since the structure includes a silicon layer. Such approaches can lead to extremely low power thresholds [34]. However, extra care must be exercised in order to retain the main advantage of the proposed structure, namely, the ultrafast response limited only by the photon lifetime in the cavity ($\tau_l \sim 1.5$ ps). The phenomena of heat or carrier diffusion are generally associated with much slower response times.

7. Acknowledgment

This work has been partially supported by the Research Committee of the Aristotle University of Thessaloniki and by the European Union (European Social Fund) and Greek national funds through the Operational Program "Education and Lifelong Learning" of the National Strategic Reference Framework: Research Funding Program THALES "Reinforcement of the interdisciplinary and/or inter-institutional research and innovation" (Project ANEMOS). The authors would like to thank Dr. Alexandros Pitilakis for fruitful discussions.

References

[1] S. I. Bozhevolnyi, ed., *Plasmonic Nanoguides and Circuits* (Pan Stanford Publishing, Singapore, 2008).

[2] O. Tsilipakos, E. E. Kriezis, and S. I. Bozhevolnyi, "Thermo-optic microring resonator switching elements made of dielectric-loaded plasmonic waveguides," J. Appl. Phys. **109**, 073111 (2011).

[3] J. A. Dionne, K. Diest, L. A. Sweatlock, and H. A. Atwater, "PlasMOStor: A metal-oxide-Si field effect plasmonic modulator," Nano Lett. **9**, 897–902 (2009).

[4] K. F. MacDonald, Z. L. Samson, M. I. Stockman, and N. I. Zheludev, "Ultrafast active plasmonics," Nature Photon. **3**, 55–58 (2009).

[5] C. Milián and D. V. Skryabin, "Nonlinear switching in arrays of semiconductor on metal photonic wires," Appl. Phys. Lett. **98**, 111104 (2011).

[6] A. Kriesch, D. Ploss, J. Wen, P. Banzer, and U. Peschel, "Nonlinear effects in subwavelength plasmonic directional couplers," in "*CLEO 2012: Conference on Lasers and Electro-Optics*," paper 6327055.

[7] A. Pitilakis and E. E. Kriezis, "Highly nonlinear hybrid silicon-plasmonic waveguides: analysis and optimization," J. Opt. Soc. Am. B **30**, 1954–1965 (2013).

[8] V. R. Almeida and M. Lipson, "Optical bistability on a silicon chip," Opt. Lett. **29**, 2387–2389 (2004).

[9] A. Pannipitiya, I. D. Rukhlenko, and M. Premaratne, "Analytical theory of optical bistability in plasmonic nanoresonators," J. Opt. Soc. Am. B **28**, 2820–2826 (2011).

[10] X. Wang, H. Jiang, J. Chen, P. Wang, Y. Lu, and H. Ming, "Optical bistability effect in plasmonic racetrack resonator with high extinction ratio," Opt. Express **19**, 19415–19421 (2011).

[11] G. Wang, H. Lu, X. Liu, Y. Gong, and L. Wang, "Optical bistability in metal-insulator-metal plasmonic waveguide with nanodisk resonator containing Kerr nonlinear medium," Appl. Opt. **50**, 5287–5290 (2011).

[12] Y. Xiang, X. Zhang, W. Cai, L. Wang, C. Ying, and J. Xu, "Optical bistability based on Bragg grating resonators in metal-insulator-metal plasmonic waveguides," AIP Advances **3**, 012106 (2013).

[13] M. Wu, Z. Han, and V. Van, "Conductor-gap-silicon plasmonic waveguides and passive components at subwavelength scale," Opt. Express **18**, 11728–11736 (2010).

[14] A. Pitilakis, O. Tsilipakos, and E. E. Kriezis, "Nonlinear effects in hybrid plasmonic waveguides," in "*ICTON 2012: 14th International Conference on Transparent Optical Networks* (IEEE, 2012)," paper 6254436.

[15] B. Esembeson, M. L. Scimeca, T. Michinobu, F. Diederich, and I. Biaggio, "A high-optical quality supramolecular assembly for third-order integrated nonlinear optics," Adv. Mater. **20**, 4584–4587 (2008).

[16] C. Koos, P. Vorreau, T. Vallaitis, P. Dumon, W. Bogaerts, R. Baets, B. Esembeson, I. Biaggio, T. Michinobu, F. Diederich, W. Freude, and J. Leuthold, "All-optical high-speed signal processing with silicon-organic hybrid slot waveguides," Nat. Photon. **3**, 216–219 (2009).

[17] P. B. Johnson and R. W. Christy, "Optical constants of the noble metals," Phys. Rev. B **6**, 4370–4379 (1972).

[18] B. A. Daniel and G. P. Agrawal, "Vectorial nonlinear propagation in silicon nanowire waveguides: polarization effects," J. Opt. Soc. Am. B **27**, 956–965 (2010).

[19] O. Tsilipakos and E. E. Kriezis, "Microdisk resonator filters made of dielectric-loaded plasmonic waveguides," Opt. Commun. **283**, 3095–3098 (2010).

[20] D. A. Ketzaki, O. Tsilipakos, T. V. Yioultsis, and E. E. Kriezis, "Electromagnetically induced transparency with hybrid silicon-plasmonic traveling-wave resonators," J. Appl. Phys. **114**, 113107 (2013).

[21] J. Bravo-Abad, S. Fan, S. Johnson, J. D. Joannopoulos, and M. Soljačić, "Modeling nonlinear optical phenomena in nanophotonics," J. Lightw. Technol. **25**, 2539–2546 (2007).

[22] M. Soljačić, M. Ibanescu, S. G. Johnson, Y. Fink, and J. D. Joannopoulos, "Optimal bistable switching in nonlinear photonic crystals," Phys. Rev. E **66**, 055601 (2002).

[23] M. F. Yanik, S. Fan, and M. Soljačić, "High-contrast all-optical bistable switching in photonic crystal microcavities," Appl. Phys. Lett. **83**, 2739–2741 (2003).

[24] B. Maes, P. Bienstman, and R. Baets, "Switching in coupled nonlinear photonic-crystal resonators," J. Opt. Soc. Am. B **22**, 1778–1784 (2005).

[25] O. Tsilipakos, A. Pitilakis, A. C. Tasolamprou, T. V. Yioultsis, and E. E. Kriezis, "Computational techniques for the analysis and design of dielectric-loaded plasmonic circuitry," Opt. Quantum Electron. **42**, 541–555 (2011).

[26] M. Notomi, "Manipulating light with strongly modulated photonic crystals," Rep. Prog. Phys. **73**, 096501 (2010).

[27] H. A. Haus, *Waves and Fields in Optoelectronics* (Prentice-Hall, New Jersey, 1984).

[28] B. E. Little, S. T. Chu, H. A. Haus, J. Foresi, and J.-P. Laine, "Microring resonator channel dropping filters," J. Lightw. Technol. **15**, 998–1005 (1997).

[29] S. Fan, W. Suh, and J. D. Joannopoulos, "Temporal coupled-mode theory for the Fano resonance in optical resonators," J. Opt. Soc. Am. A **20**, 569–572 (2003).

[30] E. D. Palik, ed., *Handbook of Optical Constants of Solids* (Academic Press, New York, 1985), 1st ed.

[31] B. L. Lawrence, M. Cha, J. U. Kang, W. Toruellas, G. Stegeman, G. Baker, J. Meth, and S. Etemad, "Large purely refractive nonlinear index of single crystal P-toluene sulphonate (PTS) at 1600 nm," Electron. Lett. **30**, 447–448 (1994).

[32] V. Van, T. A. Ibrahim, P. P. Absil, F. G. Johnson, R. Grover, and P.-T. Ho, "Optical signal processing using nonlinear semiconductor microring resonators," IEEE J. Sel. Topics Quantum Electron. **8**, 705–713 (2002).

[33] Q. Xu and M. Lipson, "Carrier-induced optical bistability in silicon ring resonators," Opt. Lett. **31**, 341–343 (2006).

[34] M. Notomi, A. Shinya, S. Mitsugi, G. Kira, E. Kuramochi, and T. Tanabe, "Optical bistable switching action of Si high-Q photonic-crystal nanocavities," Opt. Express **13**, 2678–2687 (2005).